**Supporting Information**

# Pore Size Effects on Surface Charges and Interfacial Electrostatics of Mesoporous Silicas

*Kento Murota* [a, b] [*], *Takumi Saito* [c]

a Department of Nuclear Engineering and Management, School of Engineering, The University of Tokyo, 7-3-1 Hongo, Bunkyo-ku, Tokyo 113-8656, Japan

b Regulatory Standard and Research Department, Secretariat of Nuclear Regulation Authority, 1-9-9 Roppongi, Minato-ku, Tokyo 106-8450, Japan

c Nuclear Professional School, School of Engineering, The University of Tokyo, 2-22 Shirakata Shirane, Tokai-mura, Naka-gun, Ibaraki 319-1188, Japan

* E-mail: murota@radw.t.u-tokyo.ac.jp

**Method for nitrogen gas adsorption**

First, a sample of about 0.2 g was dried at either 120 °C for 6 hours or at 350 °C for 8 hours. The different pretreatment temperatures were tested as the pore structure of SBA-15 has been reported to change under high-temperature treatment.[1] The results showed that there was no difference in the overall pore distributions and specific surface areas, although there was a slight difference in the region of very small pores of less than 1 nm in diameter. After the pretreatment, the amount of adsorbed $N_2$ was measured as a function of pressure at 77.15 K. The equilibrium time at each point was until the pressure change was less than 5 mmHg or 5% every 10 seconds. The adsorption isotherms during desorption were also measured by decreasing the pressure after the relative pressure reached 0.995, and the presence of hysteresis was investigated. The measurements were verified to be accurate by measuring a silica-alumina standard sample with known specific surface area and pore size distribution. The DFT method optimized for MCM-41 and similar mesoporous silicas was used to analyze the specific surface area and pore distribution.[2] The range of isotherms up to a relative pressure of 0.9 was used for the analyses. For comparison, the BET method was also used for the analyses of the specific surface area, and the BJH method was used for the analyses of the pore distribution using the thickness curve equation and the correction to the Kelvin equation (KJS method) proposed by Kruk et al.[3] In addition, the specific surface area of external surface was evaluated by the t-plot method, which is known to be effective for samples containing micropores. [4,5] Because the thickness curve equation in the KJS method is limited in the range of applicable relative pressures, the thickness of the adsorbed layer in the t-plot was obtained from the gas adsorption data of a silica without mesopores or micropores reported by Jaroniec et al.[6] In the t-plot method, when the amount of gas adsorbed is plotted as a function of the thickness of the adsorbed layer, the slope of the linear

2

portion in the pressure range after capillary condensation occurs corresponds to the surface area

of the external surface.

**Method for measurement of the dissolved silicic acid**

   To estimate the time required for the dissolution equilibrium, a 20 mg sample of silica was dispersed in 5 ml of liquid phases (4 g/l solid-liquid ratio) with ionic strengths adjusted to 50 mM by the addition of 0.05 ml of an 0.1 mM $HNO_3$ solution and 0.245 ml of a 1 M $NaNO_3$ solution. After 1, 3, 5, and 7 days, the liquid phases were removed by centrifugation at 10,776 g for 10 min (Kubota Model 7000, A-6512C rotor), and the Si concentrations were measured. The speed and time of centrifugation were the same thereafter. Next, the amount of released silicic acid at different pH levels was examined, where 20 mg of silica sample was dispersed in 5 ml of liquid phases with the pH adjusted from pH 8 to 10 and with the ionic strength adjusted to 50 mM using NaOH and $NaNO_3$ solutions. The Si concentrations in the liquid phases were measured after 5 days. This 5-day period corresponds to the period required for the dissolved silica to reach equilibrium, as described below. All batch experiments were conducted in ambient atmosphere at room temperature (20-25 °C) and containers were continuously agitated with a shaker. The concentration of silicic acid in the liquid phase was determined by the Molybdate yellow method.[7] An ammonium molybdate solution was added to aliquots of the liquid phases after adjusting the pH to below 2, and the absorbances at 410 nm were measured with a UV-vis spectrometer (UV-2700, Shimadzu Corporation).

**Adsorption and desorption isotherms of nitrogen**

Figure S1 shows the adsorption and desorption isotherms of nitrogen at 77.15 K on/from the mesoporous silica. Here, each sample name is denoted by combining the first letter of the name of the silica (MCM-41 or SBA-15) with the mesopore diameter determined by the DFT method, as in the main text. It can be seen that M12.4 has more saturated adsorption and larger pores than the other mesoporous silicas. For all of the samples except M3.4, the adsorption and desorption isotherms are different in some sections, indicating the presence of hysteresis in nitrogen adsorption. This hysteresis can be caused by the rapid release of condensed (liquefied) gas in the presence of mesopores larger than 3.8 nm in diameter (in the case of N2 77 K).[8] In pores smaller than 3.8 nm in diameter, condensation and evaporation occur reversibly because the influence of the surface grows stronger and the hemispherical meniscus becomes unstable. This accords with the result showing that hysteresis was almost entirely absent in M3.4. For M6.8, S7.1, and S7.9, the relative pressure at which the hysteresis ended and the adsorption and desorption isotherms overlapped was about 0.45, indicating the possibility of a "tensile strength effect". This effect may have been due to the existence of pores larger than 3.8 nm in diameter (the threshold for capillary condensation), and also to the fact that nitrogen in such pores is not desorbed until the relative pressure is about 0.45. If the effect occurs, the isotherm of the adsorption branch must be used to analyze the pore distribution.[8] Therefore, the isotherms of the adsorption branch were used for all of the samples in the further analysis. An earlier report states that the isotherm of the desorption branch should be used for the DFT method, as the method cannot properly represent capillary condensation for samples with pores smaller than 5 nm in diameter and small hysteresis loops.[9] As shown in Figure S1, however, no such samples exist, and the use of the isotherm of the adsorption branch for the DFT method is appropriate.
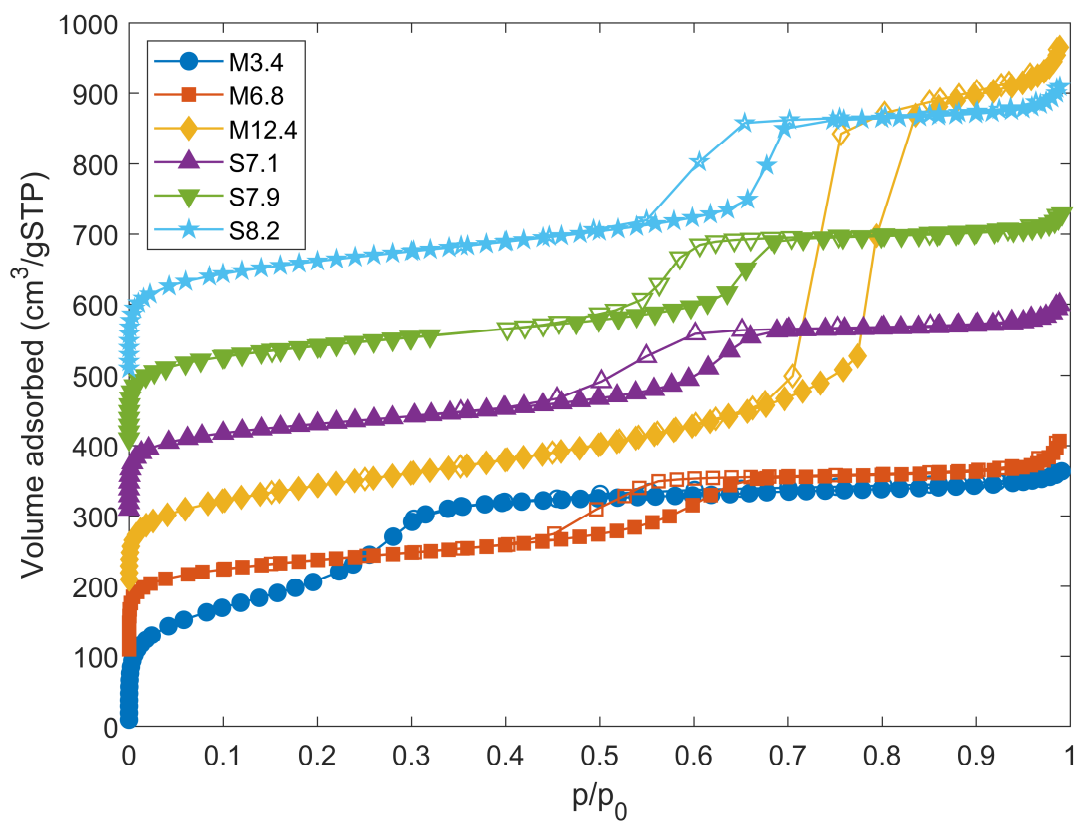
5

**Figure S1.** Adsorption (filled dots) and desorption (white dots) isotherms of nitrogen at 77.15 K on the mesoporous silicas. Each isotherm is offset in 100 cm$^3$/gSTP to make it easier to see.

**Comparison between the BJH and DFT methods**

Figure S2 shows the pore distribution of mesoporous silica determined by the BJH and DFT methods. For M3.4, both methods show the presence of mesopores in the range from 3 to 4 nm in diameter. For the other silicas, the distributions of mesopores determined by the BJH method are shifted to the left of the distributions determined by the DFT method. The equation of the thickness curve and correction for the Kelvin equation of the KJS method used in this study were derived from gas adsorption tests and XRD analysis of MCM-41, which has no micropores.[3] Therefore, the pore distribution of M3.4 (which is also almost entirely free from micropores) determined by the BJH method was consistent with that determined by the DFT method, whereas the pore sizes of the other samples containing micropores determined by the BJH method were underestimated compared to those determined by the DFT method. This agrees well with an earlier study demonstrating that the methods for determining the pore distribution using the Kelvin equation, such as the BJH method, underestimate the pore size of mesopores smaller than 10 nm in diameter.[10] In addition, unlike the BJH method, the DFT method has the advantage of being able to analyze the distribution of micropores.
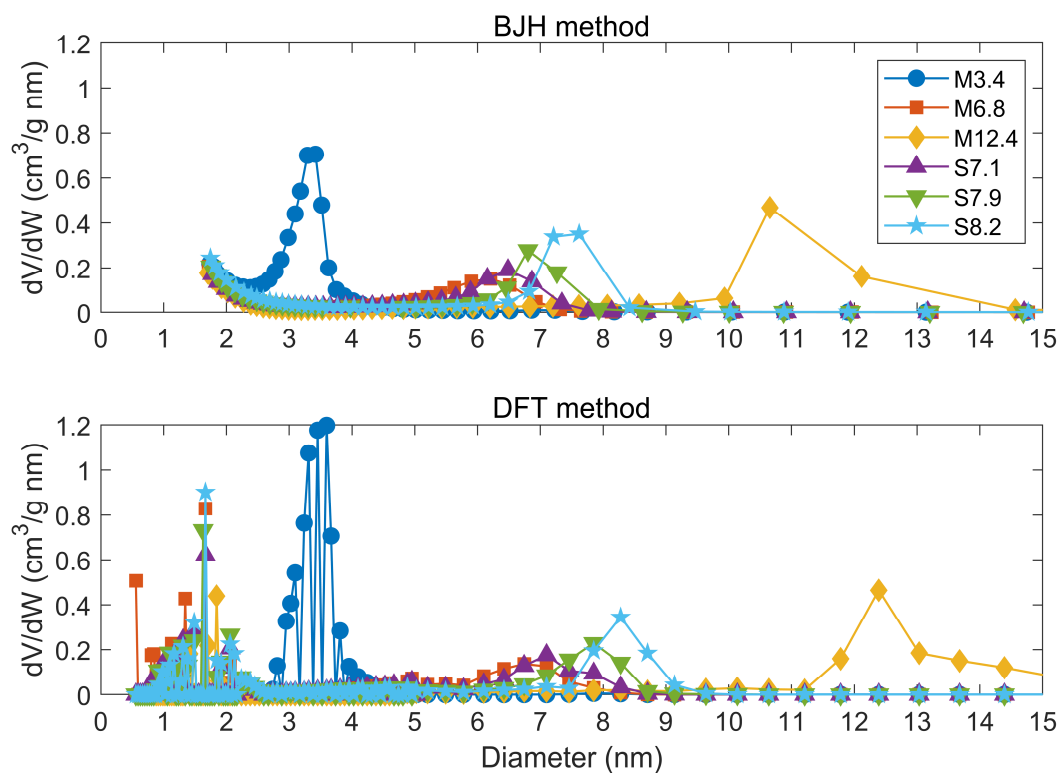
**Figure S2.** Pore distribution of the mesoporous silicas determined by the BJH and DFT methods.

**Applicability of the BET method**

For comparison with the DFT method, the BET method was also used to calculate the specific surface area. Its application, however, is problematic for the following reasons. First, the characteristics of the samples may leave some assumptions of the BET method unsatisfied. For materials containing both micropores and mesopores (or outer surfaces), such as the samples in this study, the BET method cannot reliably estimate the specific surface area even if the correct relative pressure range is used. The adsorption energy of the gas for each is different, and the molecular arrangement and molecular cross-sectional area of the gas in the micropores are unknown.[11] In addition, it has been reported that for silica, including mesoporous silica, the relative pressure at which only a monolayer of nitrogen is formed is unclear.[12] As a consequence, the BET specific surface area obtained using the nitrogen adsorption results is overestimated.[12] Second, the relative pressure range to be used for the BET method is difficult to determine. A relative pressure range of 0.05-0.35 is generally proposed for the BET method, while the method of Rouquerol et al.[11] has been known to be useful for samples with small pores.[10] However, as shown in Figure S3, the relative pressure range obtained by the method of Rouquerol et al. for M3.4, i.e., the range where the product of Q (adsorbed nitrogen amount ) and 1-p/p$_0$ (relative pressure) monotonically increases, is less than 0.31, whereas a linear relationship is observed for smaller relative pressures. This may be explainable, as the N$_2$ adsorption amount on M3.4 increases significantly from a relative pressure of about 0.2, suggesting that capillary condensation occurs at this relative pressure (see Figure S1). A range of relative pressure of 0.05-0.15 was considered to be an option for the BET method for this silica, and the linear approximation for this range is shown by the solid blue line in Figure S3. The BET specific surface area of M3.4 obtained from this line is 736 m$^2$/g. On the other hand, Figure S3 shows a linear relationship with a different slope for a smaller relative

pressure range of 0.001-0.05 (red dashed line in Fig. S3), and the BET specific surface area

obtained from this line is 612 m²/g, indicating that a large difference may appear in the specific

surface area obtained, depending on the relative pressure range used. Table S1 shows the BET

specific surface area of each silica in the relative pressure range determined by the method of

Rouquerol et al. (or $p/p_0= 0.05$-$0.15$ only for M3.4), and $p/p_0= 0.001$-$0.05$, respectively. For all the

silicas, the BET specific surface areas obtained in the smaller relative pressure range are smaller

than the BET specific surface areas using the commonly used relative pressure range. Most of the

latter values are close to those obtained by the DFT method. For M6.8, however, the specific

surface area obtained by the DFT method is larger, probably due to the effect of a particularly small

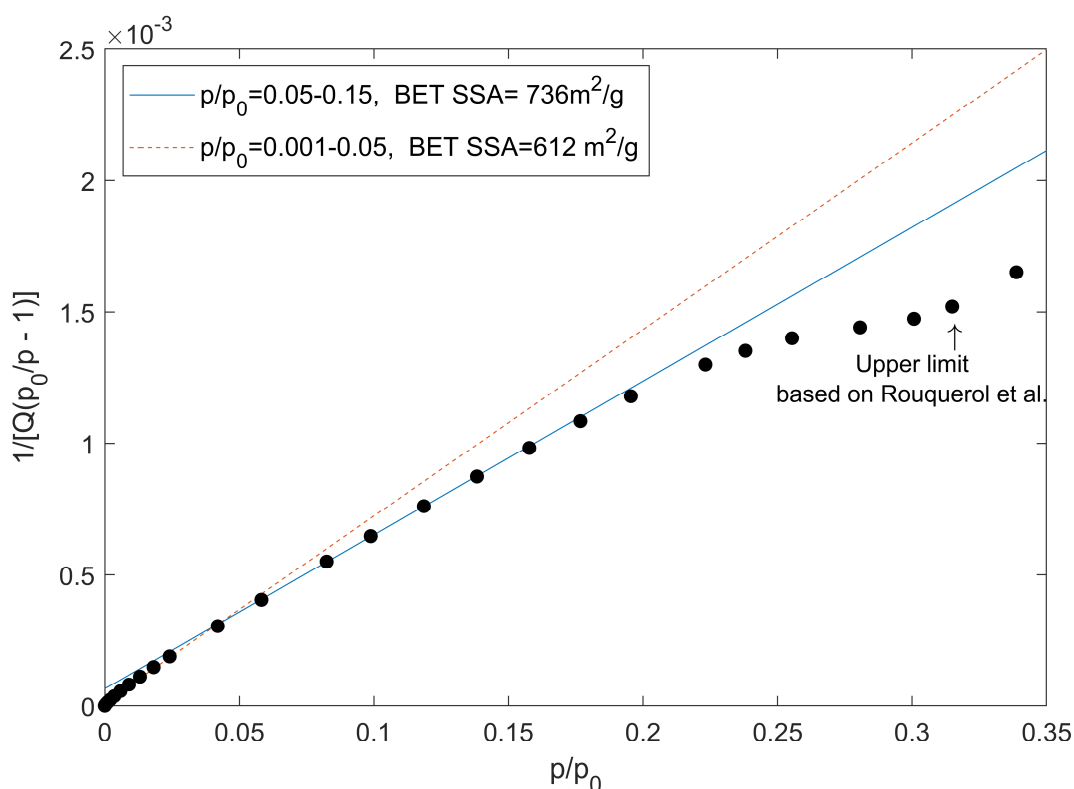micropore of 0.5 nm in diameter (Figure 1 in the main text).



**Figure S3.** BET plots for MCM-41 with mesopores of 3.4 nm in diameter. The upper limit of the

relative pressure determined based on the method of Rouquerol et al.[11] is indicated by an arrow. The solid blue line is a linear approximation of BET plots in the relative pressure range of 0.05-0.15, and the dashed red line is a linear approximation in the relative pressure range of 0.001-0.05. The BET specific surface areas obtained from each approximation are shown in the legend.

**Table S1.** BET specific surface areas determined using different relative pressure ranges.

| | MCM-41 | | | SBA-15 | | |
| --- | --- | --- | --- | --- | --- | --- |
| | M3.4 | M6.8 | M12.4 | S7.1 | S7.9 | S8.2 |
| BET specific surface area ($m^2$/g) p/p$_0$: 0.05-[a] | 736 [b] | 497 | 516 | 476 | 509 | 584 |
| BET specific surface area ($m^2$/g) p/p$_0$: 0.001-0.05 | 612 | 474 | 443 | 448 | 472 | 539 |

a: the upper limits of the relative pressure for determination of the BET specific surface area were based on Rouquerol et al.[11]
b: the upper limit of the relative pressure for determination of the BET specific surface area was set to 0.15.

**Relatively high specific surface area of external surface of M12.4**

Figure S4 shows the t-plots and the approximate straight lines used to derive the specific surface areas of the outer surfaces for M12.4 and M3.4 for comparison. For M3.4, capillary condensation occurs at the thickness of the adsorbed layer of about 0.6 nm (corresponding to a relative pressure of about 0.25), and the amount of adsorption increases in a cleanly linear fashion from the thickness of the adsorbed layer of about 1.0 nm (corresponding to a relative pressure of about 0.7). On the other hand, for M12.4, capillary condensation does not occur until high pressure compared to other silicas, and the thickness of the adsorption layer (i.e., relative pressure) where all pores are filled with nitrogen gas is not clear. In Figure S4, the specific surface area of the external surface was calculated using a range of the thicknesses greater than 1.4 nm (corresponding to a relative pressure of about 0.9), but the value of the specific surface area of the external surface varies with the choice of this range. These may be due to the fact that M12.4 has a larger mesopore diameter than the other silicas and a wider mesopore size distribution to about 20 nm in size, as clearly shown in Figure 1 in the main text.
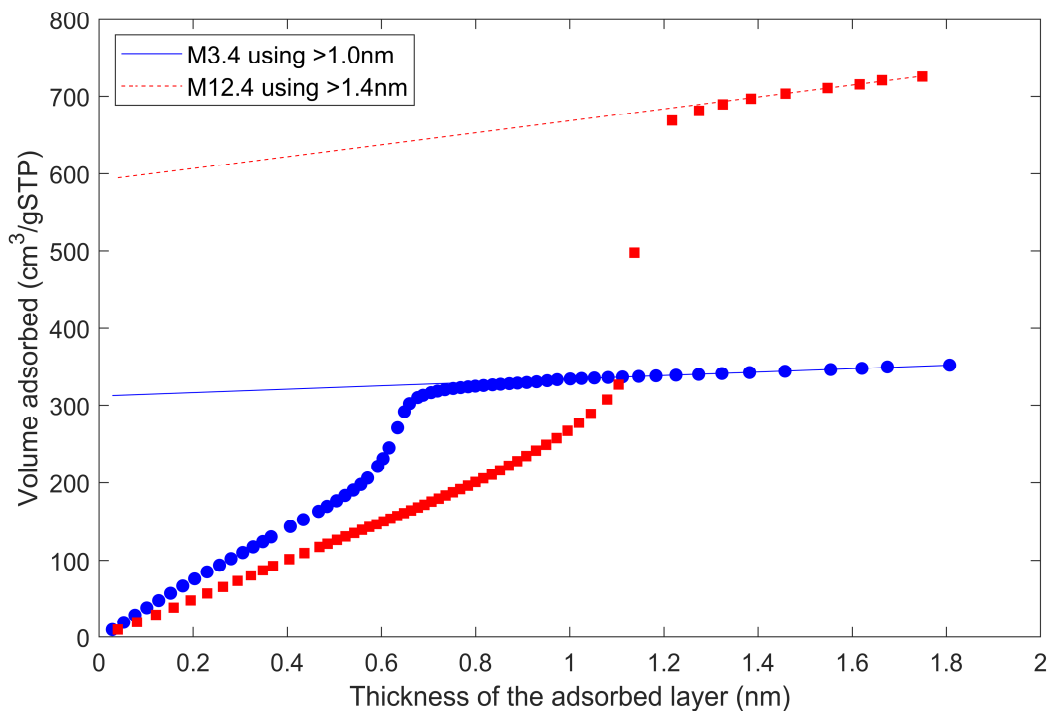
**Figure S4.** t-plots for MCM-41 with mesopores of 3.4 nm (blue circles) and 12.4 nm (red squares) in diameter. The solid blue line is a linear approximation of t-plots of MCM-41 with mesopores of 3.4 nm in diameter in the range of the thickness of the adsorbed layer over 1.0 nm, and the dashed red line is a linear approximation of t-plots of MCM-41 with mesopores of 12.4 nm in diameter in the range of the thickness of the adsorbed layer over 1.4 nm.

**The surface hydroxyl group densities of the mesoporous silicas**

When mesoporous silica is heated, the free water physically adsorbed in the pores is initially released. Next, the structural water is released through the breaking of the hydroxyl groups on the surface. Since one water molecule is released from two hydroxyl groups in the latter step, the amount of released structural water can be determined by TGA, which corresponds to twice as many hydroxyl groups as are present on the surface. The site density is then calculated from the following equation according to the method and correction factors given by Mueller et al.[13]

$$-OH = 0.625 \left( (-OH)_{1000\,°C} + \frac{2(m_{T_0} - m_{1000\,°C}) N_A}{M_{H_2O}\, m_{1000\,°C}\, SSA} \right) \tag{S1}$$

Here, -OH is the surface hydroxyl density, $(-OH)_{1000\,°C}$ is the surface hydroxyl density remaining even at 1000 °C, $m_{T_0}$ and $m_{1000\,°C}$ are the sample weights at the temperatures at which the physically adsorbed water desorbs completely ($T_0$) and 1000 °C, respectively, $N_A$ is Avogadro's number, $M_{H_2O}$ is the molar mass of water, and SSA is the specific surface area determined by the DFT method. The value of $(-OH)_{1000\,°C}$ was set to 0.4 sites/nm$^2$.[14] The temperature at which physically adsorbed water is perfectly removed and the dihydroxylation of the silanol groups commences has been discussed earlier.[15] In this study, however, the temperature was estimated using the results of DTA. Figure S5 shows the mass change of the mesoporous silicas as a function of temperature, expressed as a ratio of the mass to that before the temperature increase. The DTA curve of S7.1 is also shown as an example. The DTA curve has a large endothermic peak near 100 °C, which has been known to be due to the desorption of the physically adsorbed water.[15] This peak ends at about 200 °C, and the curve gradually becomes more exothermic as the temperature further rises. The TGA curve of S7.1 also shows a large decrease in mass immediately after the temperature is raised, almost no decrease in mass at about 170 °C, and a gradual decrease in mass again at about 200 °C. From these results, the temperature at which the free water of S7.1 is

completely vaporized and the vaporization of the structural water begins is considered to be about 200 °C. Similarly, the temperature at which the structural water begins to vaporize for each mesoporous silica was determined based on the temperature at which the large downward peak in the DTA curve ends and the mass loss occurs again in the TGA curve. Although the temperature was raised to 1000 °C in this measurement, it has been reported that 0.4 sites/nm$^2$ of the hydroxyl groups remain on the surface of silica even at 1000 °C.[14] Therefore, 0.4 sites/nm$^2$ were added to the density of the hydroxyl groups calculated from the temperature at which the structural water begins to vaporize. In addition, we used a correction factor of 0.625 determined by Mueller et al.[13] based on a comparison of the hydroxyl density of silicas determined by TGA and lithium aluminum hydride titration.

The density of the surface hydroxyl groups of each mesoporous silica obtained by the method based on TGA results is shown in Table 1 in the main text. The surface hydroxyl group densities are distributed between 3 and 5 sites/nm$^2$. When all Si on the surface of the silica constitutes silanol groups, the surface hydroxyl density is at its maximum. For amorphous silica, the value is known to be 4.6~4.9 sites/nm$^2$, regardless of the specific surface area.[15] Especially for M12.4 and S7.1, the densities are close to this upper limit. The values for M3.4 and M6.8 are smaller than the values for the others. It has been reported that SBA-15 with micropores has a larger surface hydroxyl density than MCM-41 without micropores,[16] and the small hydroxyl density of M3.4 is likely to be due to the scarcity of the micropores (Table 1 in the main text). While the reason for the small surface hydroxyl density of M6.8 is still unexplained, it may be that the very small micropores of this silica (0.56 nm in diameter) hindered the dehydration of the hydroxyl groups, leaving parts of them remaining on the surface even at 1000 °C (Figure 1 in the main text).
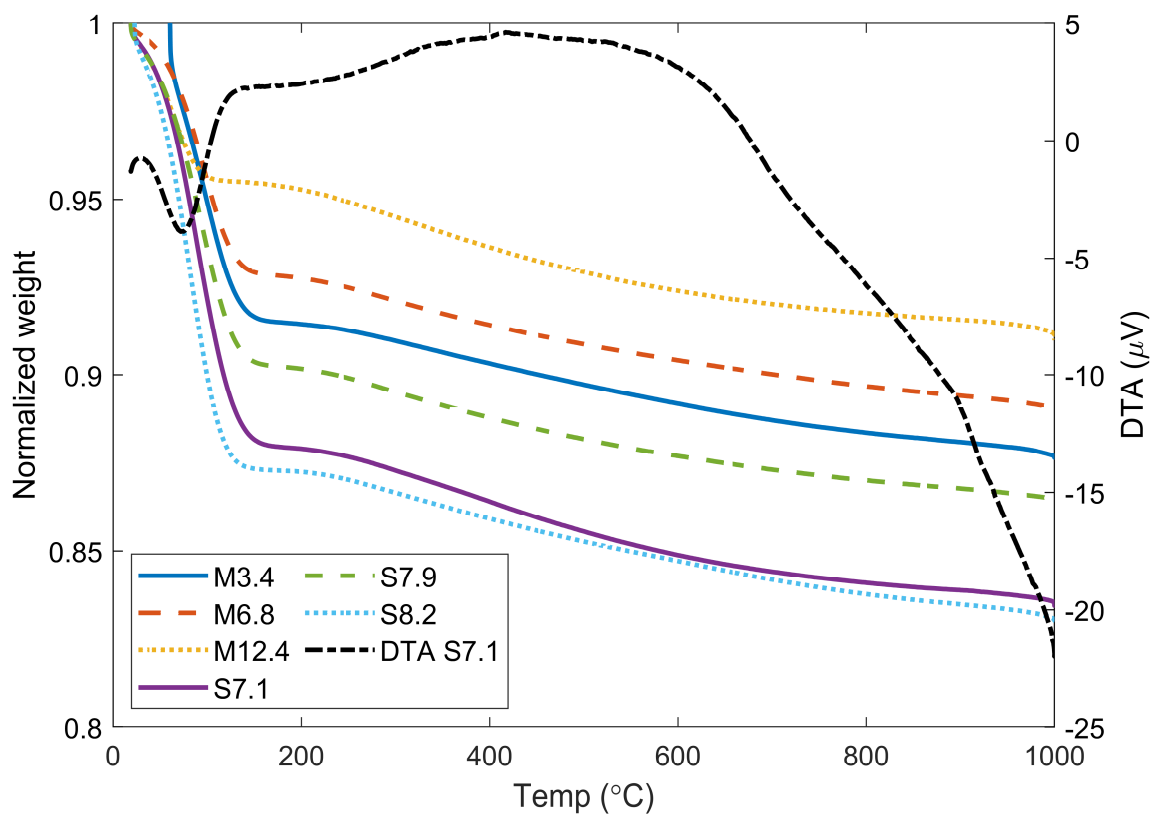
**Figure S5.** Results of the TGA and DTA analyses. The mass changes of the mesoporous silicas normalized by the masses before heating are plotted on the left axis. The voltage between SBA-15 with mesopores of 7.1 nm in diameter and the standard alumina sample is shown as a dashed black line on the right axis.

**Dissolution of the silicas**

Figure S6 shows the time variation of silicic acid concentration in the liquid phase when M3.4 and the three types of SBA-15 were dispersed in 50 mM $NaNO_3$ solutions and stirred. 1.5 to 2 mM of silicic acid was dissolved after 1 day, and the dissolution reached equilibrium after 5 days. The equilibration time was consistent with that demonstrated in similar tests previously conducted on MCM-41.[17] Although the amount of silicic acid dissolved from MCM-41 was slightly smaller than the amounts from SBA-15, about 2 mM of silicic acid was dissolved from all of the silicas at equilibrium.

Figure S7 shows the released silicic acid concentrations at different pH levels for two types of silica, M3.4 and S8.2. Also shown are the released silicic acid concentrations from amorphous silica under the same conditions, as calculated by PHREEQC ver. 3[18] based on the reactions in Table S2. No significant difference was found between MCM-41 and SBA-15 in the concentration of dissolved silicic acid at each pH. In general, MCM-41 has a thinner wall thickness between the mesopores than SBA-15 and is considered to be less chemically durable.[19] The degree of dissolution of the two could be treated similarly, however, under the conditions of this study. The measured values for MCM-41 and SBA-15 were slightly smaller than the calculated values for amorphous silica at pH 9 and above, but the trends were almost the same.
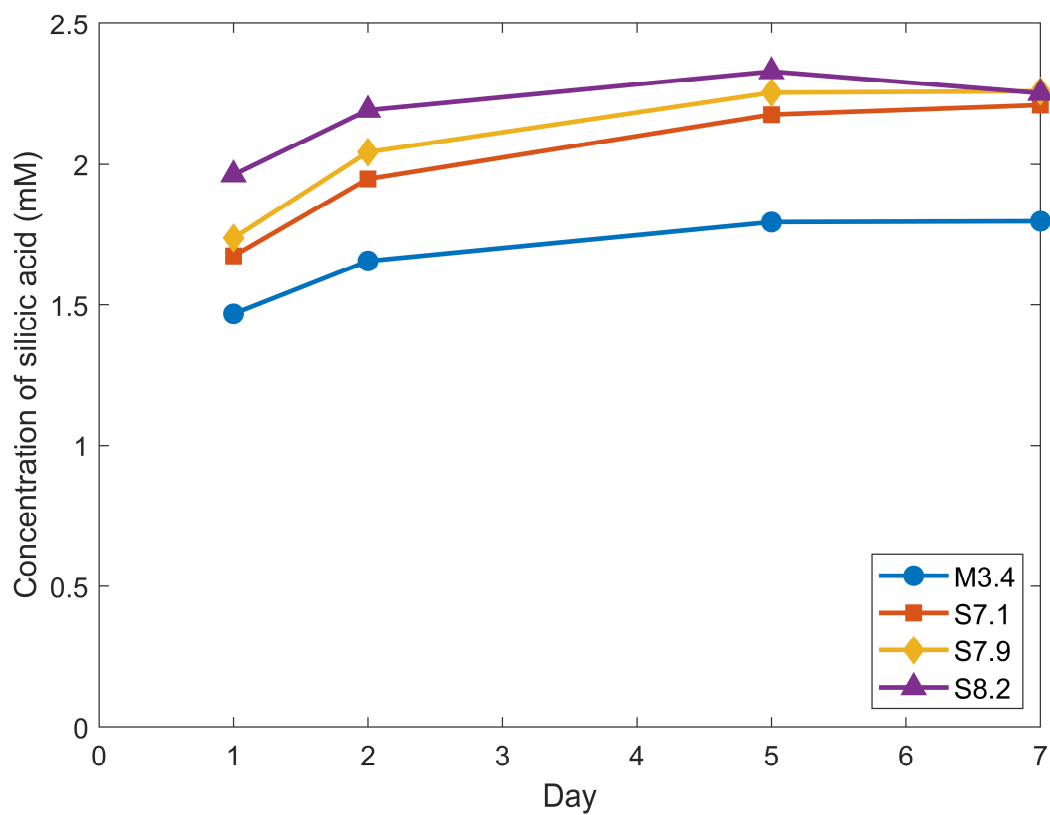
**Figure S6.** Temporal variations of the concentrations of dissolved silicic acid. The solution had an ionic strength of 50 mM, and the pH was not adjusted.
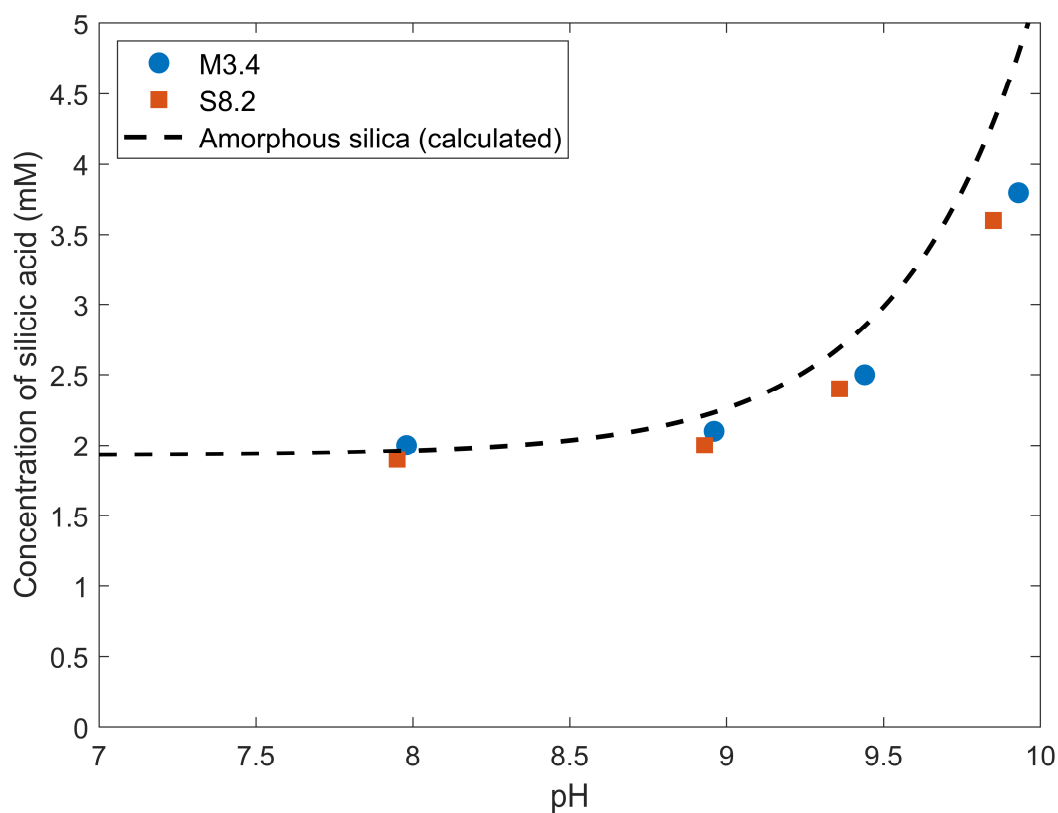
**Figure S7.** Concentrations of dissolved silicic acid from two types of mesoporous silica at different pH levels. The solution had an ionic strength of 50 mM. The dashed line represents the concentration of dissolved silicic acid from amorphous silica calculated by PHREEQC.

**Table S2.** Reactions related to the dissolution of silica.

| | log K | Reference |
|---|---|---|
| $SiO_2 + 2H_2O \rightleftharpoons Si(OH)_4$ | -2.714 [a] | Gunnarsson and Arnórsson[20] |
| $Si(OH)_4 \rightleftharpoons SiO(OH)_3^- + H^+$ | -9.81 | Thoenen et al.[21] |
| $Si(OH)_4 \rightleftharpoons SiO_2(OH)_2^{2-} + 2H^+$ | -23.14 | Thoenen et al.[21] |
| $4Si(OH)_4 \rightleftharpoons Si_4O_8(OH)_4^{4-} + 4H^+ + 4H_2O$ | -36.3 | Thoenen et al.[21] |

a: the value for amorphous silica.

**Titration curves**

Titration curves for each mesoporous silica at ionic strengths of 1, 10, and 50 mM are shown in Figure S8. The figure also shows the theoretical values of the pH change when no mesoporous silica is present in the solution. As can be seen, the presence of mesoporous silica significantly decreases the pH. This effect is due to the consumption of base in the solution when protons of the hydroxyl groups on the mesoporous silica surface dissociate and the silica has a surface charge. For all of the silicas, a decrease in the ionic strength corresponds with a greater pH increase with a smaller amount of base. In other words, silicas with lower ionic strengths have a weaker buffering effect. In comparing the mesoporous silicas, M12.4 tends to have a lower pH than the others. This tells us that M12.4 dissociates more protons than the other mesoporous silicas at the same solid-liquid ratio.
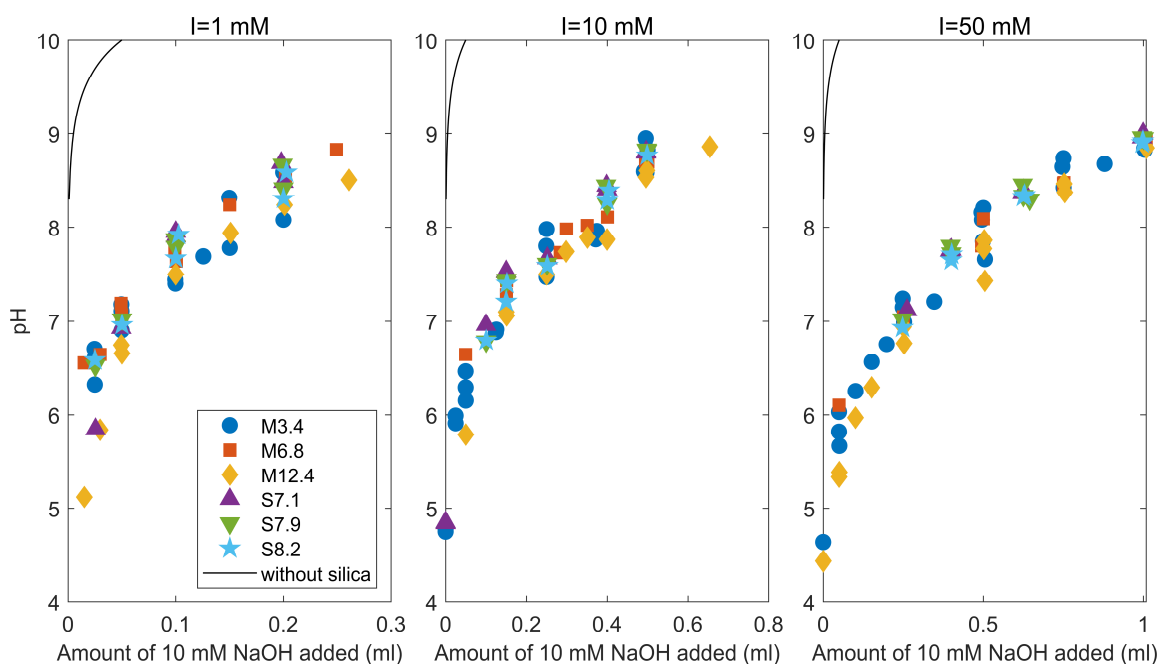


**Figure S8.** Titration curves of the mesoporous silicas at ionic strengths of 1, 10, and 50 mM. Black lines are theoretical values in the absence of mesoporous silica.

**Calculation of surface charge density**

We calculated the surface charge density from the following equation based on Goyne et al. [22]

$$\sigma_0 = \frac{F}{SSA}\frac{V}{m_{silica}}\left\{\left(\frac{K_w}{\alpha \, C_{NaOH}} - 10^{-pH}\right) - \left(\alpha \, C_{NaOH} - \frac{K_w}{10^{-pH}}\right) + \alpha \, C_{SiO(OH)_3^-}\right\} \qquad [S2]$$

Here, $\sigma_0$ is the surface charge density, F is Faraday's constant, V is the volume of solution, $m_{silica}$ is the mass of the silica, $K_w$ is the dissociation constant of water, $\alpha$ is the activity constant, and C is the concentration in solution. The activity coefficient was calculated by Davies' equation. As shown above, this study focuses on the reactions below pH 9, where the dissolution of mesoporous silica is less pronounced. Even in this range, however, we need to consider the consumption of base by dissolved silicic acid. We calculated the concentration of $SiO(OH)_3^-$, $C_{SiO(OH)_3^-}$ from the measured Si concentration determined by the molybdenum yellow method and the results of thermodynamic calculations using PHREEQC ver. 3,[18] based on the close relationship between the measured concentrations of silicic acid released from the mesoporous silicas and the value calculated using literature values for the dissolution of amorphous silica shown in Table S2. Specifically, the ratios of $C_{SiO(OH)_3^-}$ to the total concentration of Si in equilibrium with amorphous silica at different pH levels were determined by thermodynamic calculations. Using those ratios, $C_{SiO(OH)_3^-}$ in equilibrium with the mesoporous silicas at pH 8 and pH 9 was determined from the measured total concentrations of Si at pH 8 and pH 9. In the pH range below 8, the total Si concentration was assumed to be the same as the total Si concentration in the liquid phase in equilibrium with M3.4 at pH 8, and $C_{SiO(OH)_3^-}$ was determined by the above-mentioned ratios. For the pH range between 8 and 9, a linear interpolation was performed using the logarithm of $C_{SiO(OH)_3^-}$ at pH 8 and pH 9, since log $C_{SiO(OH)_3^-}$ can be regarded as proportional to the pH in this pH range. Here, as shown in Table S2, base is also consumed during the formation

of $SiO_2(OH)_2^{2-}$ and $Si_4O_8(OH)_4^{4-}$. Their effects on the surface charge density are negligible, however, as their formation constants are smaller than those for $SiO(OH)_3^-$, and they are rarely formed in the pH range of interest in this study.

Taking M12.4 as an example, Figure S9 shows how the pH change caused by the silicic acid released from the silica affects the calculated surface charge densities. As the pH increased, the proton dissociation reaction of silicic acid proceeded, and the absolute value of surface charge density decreased compared to the case where the effect was disregarded. Since the dissolution of the silica was independent of ionic strength, the effect was particularly pronounced at the ionic strength of 1 mM, where the absolute value of the surface charge density was small.
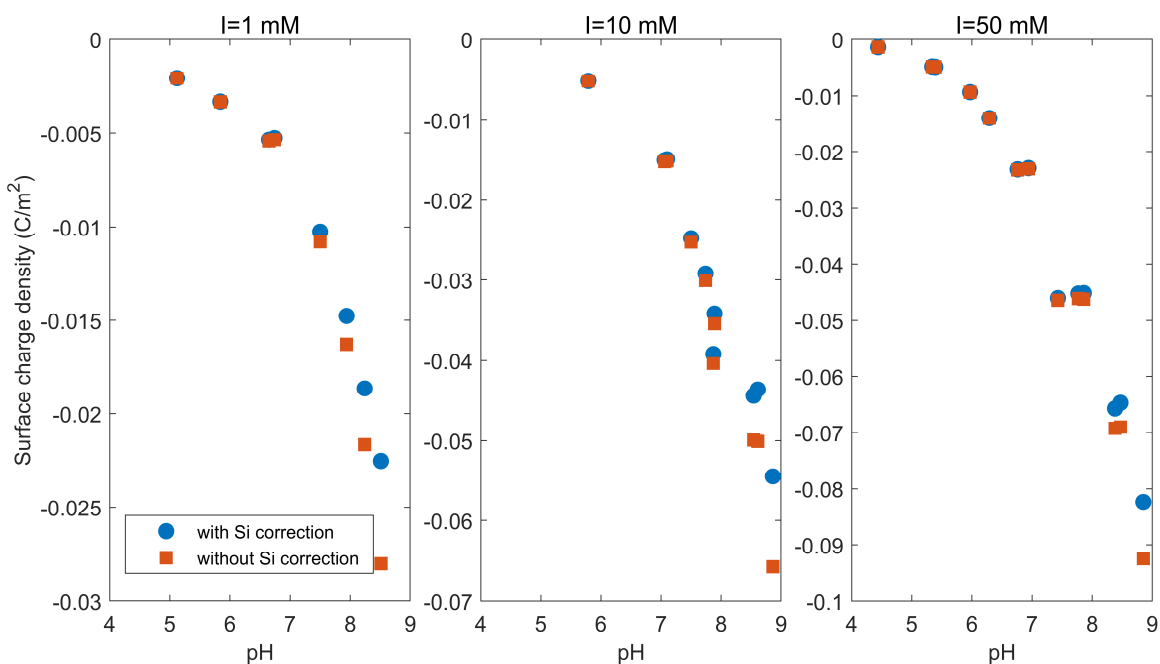


**Figure S9.** Surface charge densities of MCM-41 with mesopores of 12.4 nm in diameter. Values that take into account the proton dissociation reaction of silicic acid released from the silica (blue circles), and values that ignore the reaction (red squares).

**Representative values for surface charge density**

**Table S3.** Surface charge densities of the mesoporous silicas at ionic strengths (I) of 1, 10, and 50 mM and pH about 7 and 8.5. The numbers in parentheses are the actual pH values.

| | MCM-41 | | | SBA-15 | | |
|---|---|---|---|---|---|---|
| [C/m$^2$] | M3.4 | M6.8 | M12.4 | S7.1 | S7.9 | S8.2 |
| **pH 7** | | | | | | |
| I=1 mM | -0.0036 (6.90) | -0.0036 (7.07) | -0.0053 (6.74) | -0.0049 (6.93) | -0.0047 (7.02) | -0.0042 (6.96) |
| I=10 mM | -0.0087 (6.91) | -0.0102 (7.28) | -0.0151 (7.06) | -0.0094 (6.96) | -0.0090 (6.78) | -0.0081 (6.79) |
| I=50 mM | -0.016 (6.99) | -0.016 (7.05) | -0.023 (6.94) | -0.023 (7.12) | -0.020 (7.02) | -0.018 (6.93) |
| **pH 8.5** | | | | | | |
| I=1 mM | -0.018 (8.56) | -0.011 (8.55) | -0.023 (8.51) | -0.015 (8.49) | -0.015 (8.42) | -0.012 (8.59) |
| I=10 mM | -0.030 (8.59) | -0.029 (8.70) | -0.044 (8.54) | -0.034 (8.45) | -0.032 (8.45) | -0.030 (8.40) |
| I=50 mM | -0.045 (8.43) | -0.044 (8.48) | -0.065 (8.47) | -0.051 (8.40) | -0.047 (8.46) | -0.044 (8.35) |

**Application of the PB equation to the model**

In general surface complexation models, the target solid surface is regarded as an infinite plate, and the relationship between the charge and potential is derived using the analytical solution of the PB equation that exists in the case of a planar surface.[23] In this study we model the surface reaction in a small pore in mesoporous silica, and we model the potential on the pore surface by the following cylindrical one-dimensional PB equation

$$\frac{d^2\psi}{dr^2}+\frac{1}{r}\frac{d\psi}{dr}=-\frac{e}{\varepsilon_0\varepsilon_r}\sum_{i=1}^{N}z_i n_i \exp\left(-\frac{z_i F\psi}{RT}\right) \qquad [S3]$$

where $\psi$ is the electric potential in the diffuse layer, r is the radial position, e is the electrical element, $\varepsilon_0$ is the electrical constant (the dielectric constant of the vacuum), $\varepsilon_r$ is the dielectric constant of water (using the bulk value of 78.54), $z_i$ and $n_i$ are the charge number and number density of ion i, respectively, R is the gas constant, and T is the temperature. The potential distribution was obtained numerically based on the following boundary conditions[24]

$$\psi_{r=d/2}=\psi_{OHP} \qquad [S4]$$

$$\frac{\partial\psi_{r=0}}{\partial r}=0 \qquad [S5]$$

where d is the pore diameter.

We intended to use the PB-based surface complexation model with the following considerations to circumvent the limitations of PB equation to some extent.

First, it has been confirmed that the PB equation is effective even under the condition where EDLs overlap. When the PB equation was compared with a dynamic model combining the PNP and Navier-Stokes equations, they agreed well when the thickness of the EDL was smaller than or equal to the pore diameter.[25] When the thickness of the EDL was about 10 times larger than the

24

pore diameter, the PB equation slightly overestimated the charge density (by about 0.3%), but the potential distributions of the two equations were almost identical.[25]

Second, we note that the PB equation has known limitations other than the overlap of the EDLs described above, and also that its application to small spaces such as mesopores and micropores targeted in this study has been discussed.[26] Some limitations that are relevant for small spaces, such as the dielectric saturation, ion size exclusion effects, and interaction (or correlation) between ions, are more pronounced near the surface, where the change in potential is significant and the concentration of ions is high. Similarly, non-electrostatic interactions with the surface, such as Van der Waals forces and hydrogen bonding, are also more effective if the ions are closer to the surface. These phenomena can be included in a continuous PB expression by combining it with the Stern layer.[27] When Wang et al.[28] compared the results of nonequilibrium molecular dynamics with the PB equation, they found that the potential distribution in the range of the diffuse layer agreed well at ionic strengths below 0.88 M. Additionally, Gaddam et al.[29] showed that the concentration of a negatively charged fluorescent dye between 0-65 nm-thick slits, measured from fluorescence, agreed well with the solutions of the PB equation. Note here that several studies in recent years have attempted to model the potential distribution and the reaction in a small space based on the PB equation, as in this study.[24,30,31]

## Calculation flow of the model

The calculations were carried out in the following order. First, the activity of each ion pair was calculated from the activity of the free ions based on the mass action law. Here, we need to take account of the effect on the surface reaction by the potential at the surface where the reaction occurs. For this reason, we used the apparent equilibrium constant shown in the following equation in our calculation of the mass action law

$$K_{app} = K_{int} \exp \left( -\frac{\Delta z F \psi_x}{RT} \right)$$ [S6]

where $K_{int}$ is the intrinsic equilibrium constant, $\psi_x$ is $\psi_0$ or $\psi_{OHP}$, and $\Delta z$ is the charge difference generated by the surface reaction. The first surface reaction considered is the deprotonation reaction of hydroxyl groups:

$$>SiOH \rightleftharpoons SiO^- + H^+$$ [S7]

This reaction occurs at the pore surface of the silicas, and was set to $logK_{int} = -7.5$. This value was derived by Himestra et al.[32] using the bond valence theory and was found to be consistent with the value calculated by Siretanu et al. [33] based on a fitting to the surface charge density obtained by an atomic force microscopy analysis of amorphous silica surfaces. There is an additional protonation reaction ($>SiOH + H^+ \rightleftharpoons SiOH_2^+$) that leads to a positive surface charge, but only one occurring at a lower pH outside the pH range of this study (we therefore ignored it for our purposes). In this way, the model becomes a so-called 1-pK model. Another surface reaction that was taken into account was the ion-pair formation of $Na^+$ with a negative surface charge:

$$>SiO^- + Na^+ \rightleftharpoons SiO\text{-}Na$$ [S8]

As mentioned earlier, this reaction occurs on OHP. $LogK_{int}$ was set to -1.9.[32]

The numerical solution of the PB equation (eq SS3) was calculated using the fourth-order method (bvp4c) function in MATLAB, with the arguments on the potential at the OHP, ionic

strength, and pore size. From the obtained potential distribution in the diffuse layer, the total charge

of the electrolyte ions in the diffuse layer, $\sigma_d$, was calculated using the following equation

$$\frac{\partial \psi_{r=d/2}}{\partial r} = -\frac{\sigma_d}{\varepsilon_0 \varepsilon_r} \qquad [S9]$$

By setting the charge density of the electrostatically adsorbed $Na^+$ as $\sigma_{Na}$, the following

electrical neutrality condition holds

$$\sigma_0 + \sigma_{Na} + \sigma_d = 0 \qquad [S10]$$

Finally, we checked whether the mass balance of each ion and the site density (using the values

in Table 1) and the charge balance at the surface and OHP were satisfied. If they were not satisfied,

we adjusted the values of the activity of each ion in the liquid phase and the potential at the surface

and OHP, and repeated the procedure to calculate the charge density based on the mass action law

and the PB equation.

**Surface charge densities for pores of different diameters as calculated by the model**
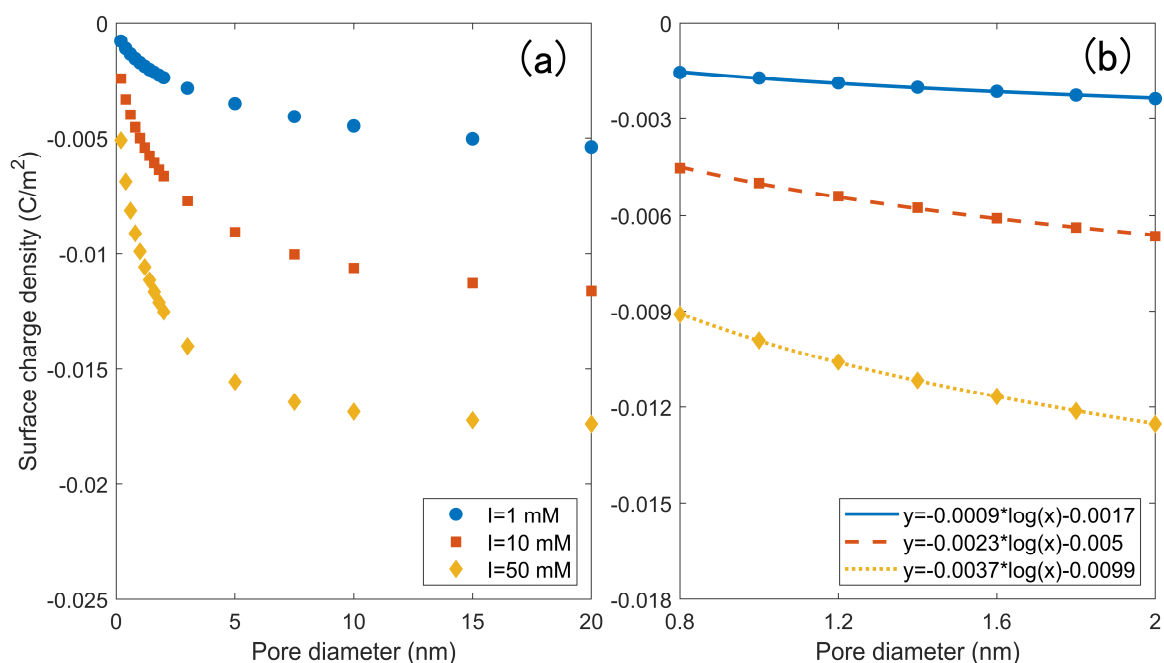


**Figure S10.** Surface charge densities for pores of different diameters at pH 7 and ionic strengths of 1, 10, and 50 mM, as calculated by the surface complexation model. The capacitance of the Stern layer and surface hydroxyl group density were set to 1 C/m$^2$ and 4 sites/nm$^2$, respectively. The pore diameter ranges are (a) 0-20 nm and (b) 0.8-2 nm. The lines in (b) are the results of the least-squares fitting of a logarithmic function of the pore diameter to surface charge densities at each ionic strength.

**Simplification of the size distribution of the specific surface areas of the silicas**

As shown in Figure 1 in the main text, the diameters of the mesopores differ between the silicas, while the micropore diameters fall uniformly in the range of 0.8-2 nm in all of the silicas but M6.8, which has a micropore diameter of 0.56 nm. Figure S10b shows a magnified view of the calculated surface charge densities for pores at different diameters (Figure 5 in the main text) within the range of 0.8-2 nm. The lines show the results of the least-squares fitting of the logarithmic function of the pore diameter to the surface charge densities in this pore diameter range. As the figure shows, the logarithmic functions can fully describe the changes in the surface charge density (R-squared over 0.99). Based on this result, 1.36 nm, an integral mean value of the logarithmic function in the range of 0.8-2, can be regarded as a representative pore diameter in the range from 0.8 to 2 nm. The surface area of each pore was defined as the surface area below 2 nm and above 2 nm in diameter, as determined by the DFT method shown in Table 1 in the main text. A comparison of the cumulative distribution of the specific surface area of S7.1, as determined from gas adsorption tests and simplified for fitting purposes, is shown in Figure S11 as an example.
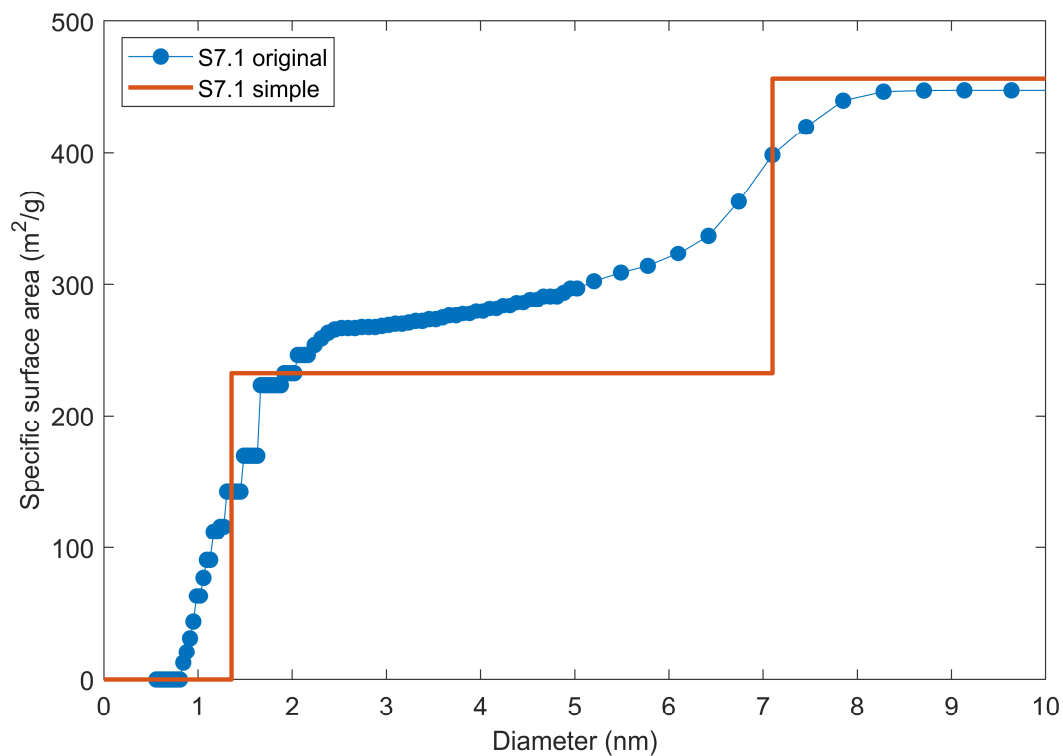
**Figure S11.** Cumulative specific surface areas of SBA-15 with mesopores of 7.1 nm in diameter. The red line is the simplified pore distribution using the original distribution (blue dots) based on the gas adsorption test analyzed by the DFT method (Figure 1 in the main text).

**Possible reasons for the large confidence interval**

The calculated surface charge densities for different Stern layer capacitances are shown in Figure S12. The absolute value of the surface charge density increases as the capacitance increases, but the increment is larger for smaller capacitances. When the capacitance increases to 5 F/m$^2$ or higher, the surface charge density hardly changes. This means that, when fitting the model to the surface charge densities by optimizing the capacitance, the change in the optimized capacitance for a small change in the surface charge densities increases more when the absolute value of the surface charge density is larger. This is likely to be the cause of the large confidence interval observed for the high capacitance. As mentioned above, the surface charge densities of the mesoporous silicas were derived by adding up the calculated surface charge values of the micropore and mesopore. Therefore, when focusing on one type of mesoporous silica, there are several combinations of Stern layer capacitances of both the micropore and mesopore that are optimal for a surface charge density of a certain value. Here, as shown in Figure 7 in the main text, the capacitance of the micropore is smaller than that of the mesopore. Therefore, a small change in the capacitance of the micropore will lead to a large change in the capacitance of the mesopore, where the extent of the capacitance change is determined by the percentage of the specific surface area occupied by the micropores.
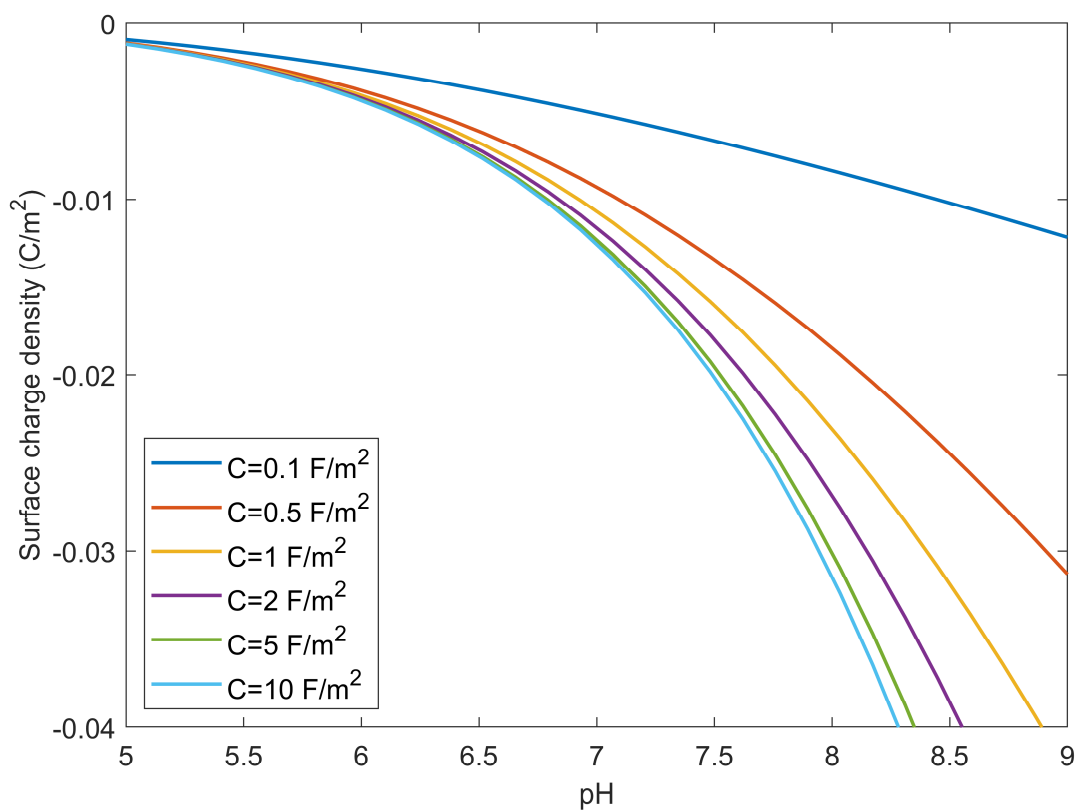
**Figure S12.** Surface charge densities of the silica pores with a pore diameter of 5 nm for different Stern layer capacitances calculated by the model. The ionic strength and surface hydroxyl group density were set to 10 mM and 4 sites/nm$^2$, respectively.

**Comparison of the optimized capacitance of the Stern layer to that of a previous study**

By fitting a model similar to the surface complexation model used in this study to the surface charge densities of silica sol, Hiemstra et al.[32] determined that the optimized capacitance of the Stern layer was 3.3 $F/m^2$. The optimized capacitances of the Stern layer with pore diameters of 6 to 8 nm and 12.4 nm obtained in this study are higher than that value. There could be two possible reasons for the discrepancy. First, there may be a size effect on the surface charge densities that Hiemstra et al. used for the fitting. The surface charge density data they used was obtained from titration tests on a spherical silica sol with a particle size of about 15 nm in diameter.[34] Not only this silica sol, but many amorphous silicas, have small particle sizes or small pores, which makes it difficult to find a comparison that has no effect of the surface curvature. Another possible reason is the treatment of surface charges developed in extremely small pore sizes in our study. In our study, we used the surface areas of pores larger than about 0.5 nm in diameter, as derived from an analysis of the $N_2$ adsorption. We could not, however, clearly determine whether the water diffusion and deprotonation reactions in the small pores of about 0.5 nm in diameter are similar to those in bigger pores. If pores smaller than a certain size do not contribute to the deprotonation reaction, then the contribution of micropores, represented by a pore diameter of 1.36 nm in the fitting, becomes small, and the optimized value of the capacitance of the Stern layer in the large pores would be smaller.

References

1    F. Bérubé and S. Kaliaguine, Calcination and thermal degradation mechanisms of triblock copolymer template in SBA-15 materials, *Microporous Mesoporous Mater.*, 2008, **115**, 469–479.

2    M. Jaroniec, M. Kruk, J. P. Olivier and S. Koch, A new method for the accurate pore size analysis of MCM-41 and other silica based mesoporous materials, *Stud. Surf. Sci. Catal.*, 2000, **128**, 71–80.

3    M. Kruk, M. Jaroniec and A. Sayari, Application of Large Pore MCM-41 Molecular Sieves To Improve Pore Size Analysis Using Nitrogen Adsorption Measurements, *Langmuir*, 1997, **13**, 6267–6273.

4    A. Galarneau, D. Mehlhorn, F. Guenneau, B. Coasne, F. Villemot, D. Minoux, C. Aquino and J. P. Dath, Specific Surface Area Determination for Microporous/Mesoporous Materials: The Case of Mesoporous FAU-Y Zeolites, *Langmuir*, 2018, **34**, 14134–14142.

5    B. Coasne, A. Galarneau, R. J. M. Pellenq and F. Di Renzo, Adsorption, intrusion and freezing in porous silica: The view from the nanoscale, *Chem. Soc. Rev.*, 2013, **42**, 4141–4171.

6    M. Jaroniec, M. Kruk and J. P. Olivier, Standard nitrogen adsorption data for characterization of nanoporous silicas, *Langmuir*, 1999, **15**, 5410–5413.

7    M. Takahashi, Y. Abe and M. Tanaka, Elucidation of molybdosilicate complexes in the molybdate yellow method by ESI-MS, *Talanta*, 2015, **131**, 301–308.

8    J. C. Groen, L. A. A. Peffer and J. Pérez-Ramírez, Pore size determination in modified micro- and mesoporous materials. Pitfalls and limitations in gas adsorption data analysis, *Microporous Mesoporous Mater.*, 2003, **60**, 1–17.

9    P. I. Ravikovitch and A. V. Neimark, Characterization of nanoporous materials from adsorption and desorption isotherms, *Colloids Surfaces A Physicochem. Eng. Asp.*, 2001, **187**–**188**, 11–21.

10    M. Thommes, K. Kaneko, A. V. Neimark, J. P. Olivier, F. Rodriguez-Reinoso, J. Rouquerol and K. S. W. Sing, Physisorption of gases, with special reference to the evaluation of surface area and pore size distribution (IUPAC Technical Report), *Pure Appl. Chem.*, 2015, **87**, 1051–1069.

11    J. Rouquerol, P. Llewellyn and F. Rouquerol, in *Studies in Surface Science and Catalysis*, 2007, vol. 160, pp. 49–56.

12    P. Selvam, S. K. Bhatia and C. G. Sonwane, Recent advances in processing and characterization of periodic mesoporous MCM-41 silicate molecular sieves, *Ind. Eng. Chem. Res.*, 2001, **40**, 3237–3261.

13   R. Mueller, H. K. Kammler, K. Wegner and S. E. Pratsinis, OH surface density of $SiO_2$ and $TiO_2$ by thermogravimetric analysis, *Langmuir*, 2003, **19**, 160–165.

14   G. Curthoys, V. Y. Davydov, A. V. Kiselev, S. A. Kiselev and B. V. Kuznetsov, Hydrogen bonding in adsorption on silica, *J. Colloid Interface Sci.*, 1974, **48**, 58–72.

15   L. T. Zhuravlev, The surface chemistry of silica - the zhuravlev model, *Colloid. Silica Fundam. Appl.*, 2005, **173**, 261–266.

16   M. Ide, M. El-Roz, E. De Canck, A. Vicente, T. Planckaert, T. Bogaerts, I. Van Driessche, F. Lynen, V. Van Speybroeck, F. Thybault-Starzyk and P. Van Der Voort, Quantification of silanol sites for the most common mesoporous ordered silicas and organosilicas: Total versus accessible silanols, *Phys. Chem. Chem. Phys.*, 2013, **15**, 642–650.

17   D. M. Singer, H. Guo and J. A. Davis, U(VI) and Sr(II) batch sorption and diffusion kinetics into mesoporous silica (MCM-41), *Chem. Geol.*, 2014, **390**, 152–163.

18   D. L. Parkhurst and C. A. J. Appelo, *Description of input and examples for PHREEQC version 3: a computer program for speciation, batch-reaction, one-dimensional transport, and inverse geochemical calculations*, Reston, VA, 2013.

19   V. Meynen, P. Cool and E. F. Vansant, Verified syntheses of mesoporous materials, *Microporous Mesoporous Mater.*, 2009, **125**, 170–223.

20   I. Gunnarsson and S. Arnórsson, Amorphous silica solubility and the thermodynamic properties of $H_4SiO_4°$ in the range of 0°to 350°C at $P_{sat}$, *Geochim. Cosmochim. Acta*, 2000, **64**, 2295–2307.

21   T. Thoenen, W. Hummel, U. Berner and E. Curti, *The PSI/Nagra Chemical Thermodynamic Database 12/07*, 2014.

22   K. W. Goyne, A. R. Zimmerman, B. L. Newalkar, S. Komarneni, S. L. Brantley and J. Chorover, Surface charge of variable porosity $Al_2O_3(s)$ and $SiO_2(s)$ adsorbents, *J. Porous Mater.*, 2002, **9**, 243–256.

23   H. Saboorian-Jooybari and Z. Chen, Analytical solutions of the Poisson-Boltzmann equation within an interstitial electrical double layer in various geometries, *Chem. Phys.*, 2019, **522**, 147–162.

24   P. Leroy and A. Maineult, Exploring the electrical potential inside cylinders beyond the Debye-Hückel approximation: A computer code to solve the Poisson-Boltzmann equation for multivalent electrolytes, *Geophys. J. Int.*, 2018, **214**, 58–69.

25   M. Wang and S. Chen, On applicability of Poisson-Boltzmann equation for micro- and nanoscale electroosmotic flows, *Commun. Comput. Phys.*, 2008, **3**, 1087–1099.

26   Z. Adamczyk, Potential Interactions Among Particles, *Interface Sci. Technol.*, 2006, **9**, 15–196.

27    J. Lyklema, in *Fundamentals of Interface and Colloid Science*, Academic Press, 1995, p. 768.

28    M. Wang, J. Liu and S. Chen, Electric potential distribution in nanoscale electroosmosis: From molecules to continuum, *Mol. Simul.*, 2008, **34**, 509–514.

29    P. Gaddam, R. Grayson and W. Ducker, Adsorption at Confined Interfaces, *Langmuir*, 2018, **34**, 10469–10479.

30    Y. Kitazumi, O. Shirai, M. Yamamoto and K. Kano, Numerical simulation of diffuse double layer around microporous electrodes based on the Poisson-Boltzmann equation, *Electrochim. Acta*, 2013, **112**, 171–175.

31    T. Gil-Díaz, D. Jara-Heredia, F. Heberling, J. Lützenkirchen, J. Link, T. Sowoidnich, H. M. Ludwig, M. Haist and T. Schäfer, Charge regulated solid-liquid interfaces interacting on the nanoscale: Benchmarking of a generalized speciation code (SINFONIA), *Adv. Colloid Interface Sci.*, , DOI:10.1016/j.cis.2021.102469.

32    T. Hiemstra, J. C. M. De Wit and W. H. Van Riemsdijk, Multisite proton adsorption modeling at the solid/solution interface of (hydr)oxides: A new approach: II. Application to various important (hydr)oxides, *J. Colloid Interface Sci.*, 1989, **133**, 105–117.

33    I. Siretanu, D. Ebeling, M. P. Andersson, S. L. S. Stipp, A. Philipse, M. C. Stuart, D. Van Den Ende and F. Mugele, Direct observation of ionic structure at solid-liquid interfaces: A deep look into the Stern Layer, *Sci. Rep.*, 2014, **4**, 19–21.

34    G. H. Bolt, Determination of the charge density of silica sols, *J. Phys. Chem.*, 1957, **61**, 1166–1169.